Telemetry Ranging: Laboratory Validation Tests and End-to-End Performance

Jon Hamkins*, Peter Kinman†, Hua Xie*, Victor Vilnrotter*, Sam Dolinar*, Norman Adams‡, Erika Sanchez‡, and Wesley Millard‡

ABSTRACT. — This article reports on a set of laboratory tests of telemetry ranging conducted at Development Test Facility 21 (DTF-21) in Monrovia, California. An uplink pseudorandom noise (PN) ranging signal was generated by DTF-21, acquired by the Frontier Radio designed and built at the Johns Hopkins University Applied Physics Laboratory, and downlink telemetry frames from the radio were recorded by an open-loop receiver. In four of the tests, the data indicate that telemetry ranging can resolve the two-way time delay to a standard deviation of 2.1 - 3.4 ns, corresponding to about 30 to 51 cm in (one-way) range accuracy, when 30 s averaging of timing estimates is used. Other tests performed worse because of unsatisfactory receiver sampling rate, quantizer resolution, dc bias, improper configuration, or other reasons.

The article also presents an analysis of the expected end-to-end performance of the telemetry ranging system. In one case considered, the theoretically-predicted performance matches the test results, within 10%, which provides a reasonable validation that the expected performance was achieved by the test. The analysis also shows that in one typical ranging scenario, one-way range accuracy of 1 m can be achieved with telemetry ranging when the data rate is above 2 kbps.

*Communications Architectures and Research Section, Jet Propulsion Laboratory, California Institute of Technology.

†California State University, Fresno.

‡Applied Physics Laboratory, Johns Hopkins University.

The research described in this publication was carried out by the Jet Propulsion Laboratory, California Institute of Technology, under a contract with the National Aeronautics and Space Administration.
© 2016 All rights reserved.

I. Introduction

Previous articles [1, 2] explained the basic concepts behind telemetry ranging, the signal processing steps required, our software implementation of those steps, and simulated performance of the individual major receiver functions on the spacecraft and the ground. In the present article, we report on a set of laboratory tests of telemetry ranging conducted at the Development Test Facility 21 (DTF-21) [3], we evaluate the ranging estimation performance of the end-to-end telemetry ranging system in relevant scenarios, and we compare the ranging estimation accuracy of the test results to theoretical predictions.

Section II describes the DTF-21 tests with the Frontier Radio, including the test goals, the hardware and software test configuration, test results, and lessons learned. Section III provides an analysis of the end-to-end performance of telemetry ranging, and compares this to the test results.

II. Laboratory Tests of Telemetry Ranging

A. Overall Test Goals

There were several high-level goals for the laboratory tests. A primary goal was to advance the Technology Readiness Level of the approach by making timing measurements in a relevant environment. A second goal was to show that an existing transponder, in the form of the Frontier Radio, needn't be substantially redesigned in order to accommodate telemetry ranging; and that ground processing, in the form of open-loop recording followed by post-processing, is sufficient to make the relevant time estimates. Since telemetry ranging involves some unusual signal processing and can be tricky to explain, a successful laboratory test can substantially reduce the risk and perceived risk of the technology.

A more detailed goal was to show that the timing estimates made in the spacecraft transponder and on the ground are consistent with the subsystem performance analysis in [2], and with the overall end-to-end performance goals of a ranging system.

B. Test facilities and equipment

1. The Frontier Radio

The Frontier Radio is a space communication and navigation radio that features low power, low mass, modularity, and a multi-band software defined modem [4]. It has been developed by the Johns Hopkins University/Applied Physics Laboratory (JHU/APL). The Frontier Radio name is not specific to an implementation of these radios, but covers the whole radio architecture platform. Two Frontier Radios are in flight on the Van Allen Probes (formally Radiation Belt Storm Probes (RBSP)) NASA mission which was launched in 2012. Currently, flight Frontier Radios are under construction for NASA's

Solar Probe Plus (SPP) mission, to be launched in 2018. Figure 1 shows a CAD model of the SPP radio. The Frontier Radio has been selected as the communications solution for NASA's upcoming Europa missions.

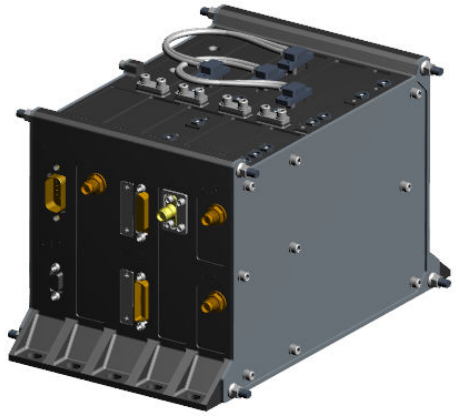

Figure 1. Frontier Radio.

The precursor to the Frontier Radio started with the development of NASA's New Horizons mission radio, circa 2000. Advances in space-grade field-programmable gate arrays (FPGAs) and up-screened commercial parts enabled the development of a new class of space radio where modularity and reconfigurability are possible. The New Horizons mission included a novel regenerative pseudorandom noise (PN) ranging implementation [5] that has been leveraged for the telemetry ranging experiment that is considered in the present study. The modular architecture of the Frontier Radio allowed telemetry ranging to be incorporated without any hardware changes and only minor changes to existing firmware [3].

Figure 2 shows a block diagram of the implementation. The clock rates of all blocks relevant to telemetry ranging are indicated by block color. The existing Frontier Radio firmware was augmented with the New Horizons PN code tracking circuit. This circuit is shown in the upper right corner of Figure 2. Two further blocks are added to enable telemetry ranging: the Latch and the Frame Edge Detector. All other blocks in Figure 2 are part of the heritage design.

A carrier recovery loop appears in the upper left corner and straddles analog and digital domains. The analog intermediate frequency (IF) is sampled coherently and the digital IF is then downconverted to baseband using a fixed digital reference. Baseband I/Q are provided to the code recovery loop. The PN code is regenerated with a sample rate of 5 MHz, and the numerically controlled oscillator (NCO) that triggers code symbols runs at 30 MHz with 35-bit precision. While the regenerated code exhibits significant jitter due to the 5-MHz code generator, the underlying code symbol phase is smoothly tracked with greater precision. The code tracking loop has a bandwidth between 0.25 Hz and 4 Hz depending upon configuration and uplink parameters.

The 12 most significant bits (MSBs) of the code symbol NCO are allocated to record symbol phase and 20 bits of the PN code generator are allocated to record a symbol number 0 through 1,009,469. The composite code phase is latched at the rising edge of the first telemetry symbol of a downlink frame. For a symbol rate of 2.068 Msps the latched code phase provides 0.12 ns resolution.

In the present study, the downlink symbol rate was chosen to be an integer divisor of the clock that drives the PN code NCO. In this case the code phase at the start of a telemetry frame can be measured directly. However, symbol rate and NCO clock need not be related in this way. If both circuits are driven by the same clock, but aren't integer divisors, then the code phase can be linearly interpolated from the neighboring NCO clock cycles. If the two circuits operate on different clocks then both the frame edge and code phase can be linearly interpolated [3].

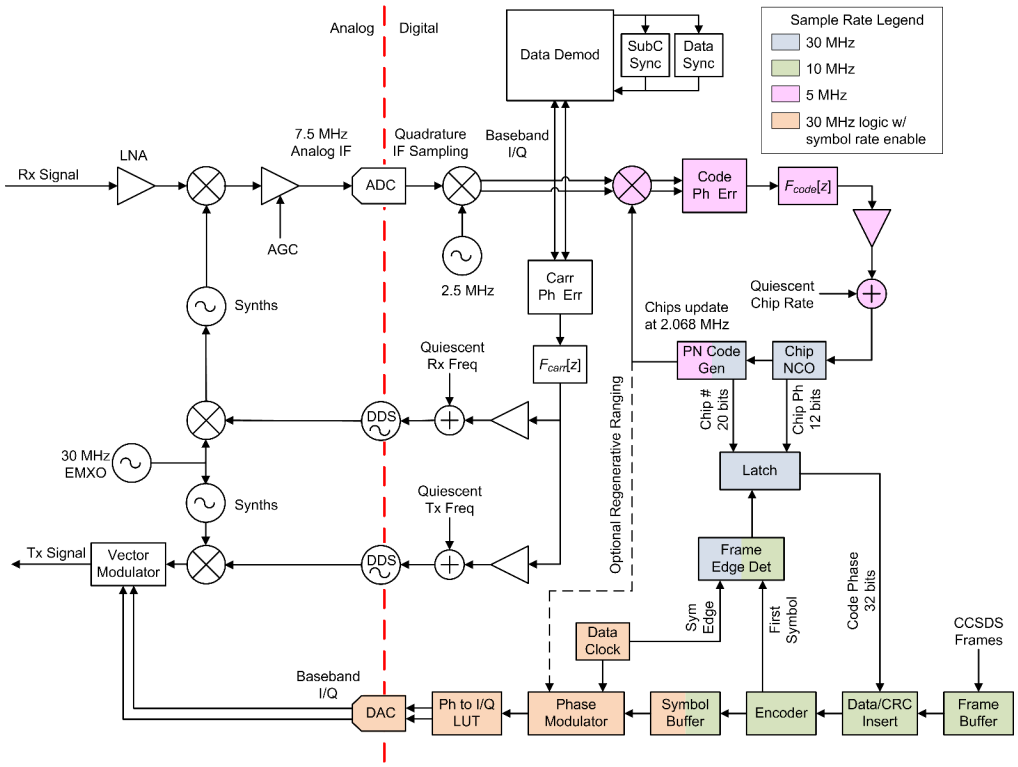

Figure 2. Frontier Radio processing for telemetry ranging.

2. DTF-21

The tests described in this article took place at DTF-21 in Monrovia, CA. DTF-21 contains simulators for Deep Space Network (DSN) antennas, transmitters, and microwave control equipment, along with a cesium beam time reference and a Block V receiver similar to those deployed in the DSN. The time references distributed throughout DTF-21 include a 100-MHz clock, and a 1 pulse per second (1-PPS) reference. DTF-21 is

used by NASA and other customers from around the world to validate and test science and communications equipment destined for installation into spacecraft or into operational ground facilities, in a realistic environment closely resembling actual operating conditions.

A block diagram of the experimental arrangement at DTF-21 is shown in Figure 3. It used an uplink carrier of approximately 7176 MHz and a downlink carrier of approximately 8431 MHz.

Both the uplink and downlink carriers were in the X band.

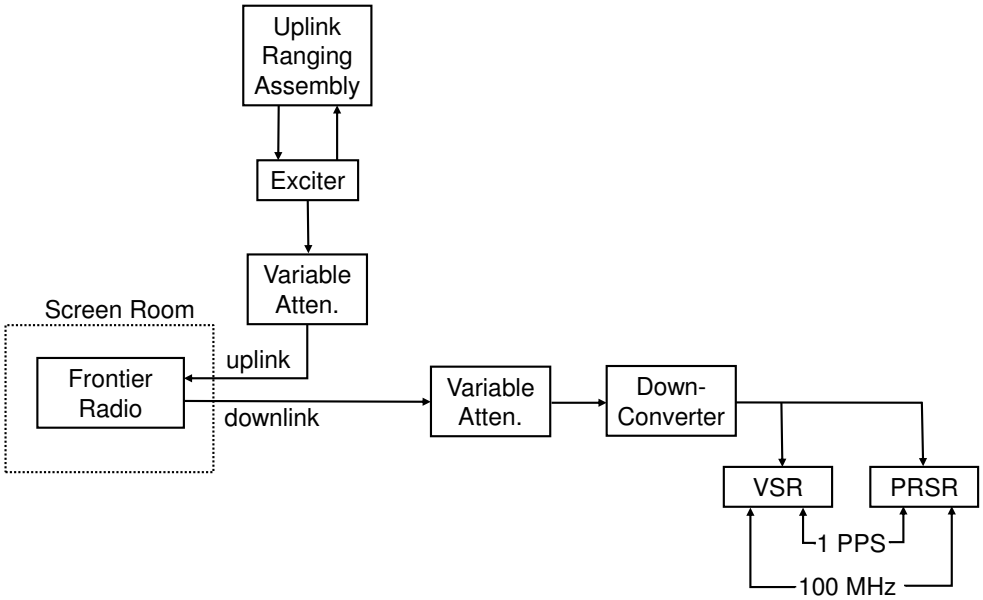

Figure 3. DTF-21 experimental arrangement.

3. Open-Loop Recorders

The Radio Science Receiver (RSR) and the VLBI Science Receiver (VSR) are open-loop recorders located on a common platform at DTF-21. For our purposes, the RSR and VSR have similar capabilities in terms of recording bandwidth and quantization levels. The VSR at DTF-21 was upgraded to full functionality in preparation for the laboratory tests.

In addition, a Portable Radio Science Receiver (PRSR) was upgraded at JPL and transported to DTF-21 as backup to the VSR, and also to provide additional capabilities for recording auxiliary data during the telemetry ranging experiments. The PRSR is a single-IF input version of the operational wideband VSR (WVSR) currently in use in the DSN and other facilities around the world. The VSR accepts IF analog signals of nominally 300 MHz (256-384 MHz), samples a 128-MHz wide band at 256 Msps with 8-bit quantization, and downconverts a 16 MHz wide channel at a user selectable center

frequency to complex baseband samples at 16 Msps with 8-bit quantization. In addition, a 100-MHz frequency reference signal and 1-PPS timing reference are also required inputs to the VSR, providing accurate timing and information and sampling clocks. Up to four subchannels with variable widths from 1 kHz to 16 MHz and sample quantization from 1 to 16 b/sample can be selected for monitoring and recording from Table 1(a).

Table 1. Allowed sample rates and quantization levels for open-loop receivers.

(a) VSR.

Subchannel Type	Sample rates	Bits of quantization
Narrowband	1, 2, 4, 8, 16, 50, 100 ksps	8, 16
Wideband	1 Msps	1, 2, 4, 8
Wideband	2 Msps	1, 2, 4, 8
Wideband	4 Msps	1, 2, 4
Wideband	8 Msps	1, 2
Wideband	16 Msps	1

(b) WVSR.

Sample rates	Bits of quantization
1, 2, 4, 8, 16, 50, 100 ksps	8, 16
1, 2, 4, 8, 16 Msps	1, 2, 4, 8
32 Msps	1, 2, 4

The data recorded by the VSR and WVSR (and hence PRSR) are preceded by identical headers that contain a precise time-tag and other auxiliary information such as sampling rate and quantization level. The time-tag for the start of the data sequence is obtained from the 1-PPS timing reference, accurate to better than 1 ns. Data recording always starts exactly on a 1-PPS marker, just as in the operational DSN, hence the start-time of the data record is known with great accuracy. It is good experimental practice to include the start-time of the data record in the file header to facilitate post-processing, and an attempt was made to name the DTF-21 files in this manner; however, this approach is subject to human error and should not be relied upon when processing these files.

Both VSR and PRSR have two basic modes of operation, called "monitoring" and "recording." Monitoring is used to set up the functions necessary for successful recording, such as fast Fourier transform (FFT) windows with various bandwidths to check the spectrum of the input signal (typically broadband and narrowband are used), and histogram windows to determine the attenuation needed to match signal levels to the input range of the analog to digital converter. For example, if the signal levels are not set correctly then the effective quantization of the signal could be compromised, in extreme cases reducing the 8-bit quantization selected by the user to effectively 1-bit

quantization. In addition, close examination of the residual carrier via narrow-band FFT can often help to identify and resolve problems in the signal chain that could compromise data quality. Once the settings have been verified via monitoring, the user can initiate recording by selecting the "enable" button on the record window, and stop recording by selecting the "disable" button.

The WVSR is an upgraded version of the aging VSR system but with two-IF inputs, and with much greater recording bandwidths and quantization capabilities than the VSR. The PRSR is a portable single-IF version of the WVSR, with identical functionality and capabilities, recording bandwidths and quantization levels, as summarized in Table 1(b).

4. Software Post-Processing

As discussed in Section VI of [2], we developed a software tool for direct processing of test data recorded by an RSR, VSR, or WVSR. The graphical user interface (GUI) for this tool is shown in Figure 21 of [2], repeated here as Figure 4. This tool provides the ground signal processing for receiving a telemetry-ranging signal recorded by an RSR, VSR, or WVSR. The GUI allows the user to select the open-loop recorder type used and the name of the file containing the recording. All of the signal processing steps described in Section VI of [2] are carried out, culminating in a sequence of $\psi_{\mathrm{S}}(t_{\mathrm{S}})$ phase measurements suitable for use in computing range.

The software saves "diaries" of the screen output from the MATLAB programs, as well as three huge variables causing the saved MATLAB workspaces to be about the same size as the test data files themselves. Comments on most of the test runs were added after analyzing the test diaries and post-processing the saved MATLAB data.

C. Signal Formats and Parameters Used in the Laboratory Tests

The uplink PN range code signal provided by DTF-21 is described by equation (3) in [2]. Parameters include the uplink carrier frequency f_c, total signal power P_t, peak modulation index ϕ_r, and PN waveform $\phi_{\mathrm{PN}}(t)$. Since the range clock and uplink carrier were to be coherently related, a reference frequency was supplied by the exciter to the Uplink Ranging Assembly, the source of the PN range code. The uplink carrier frequency f_c was approximately 7176 MHz, and the range clock was $221/(749 \cdot 2048)$ times this carrier frequency. Thus, the range clock was approximately 1 MHz. (The chip rate, with two chips per cycle of the range clock, was approximately 2 Mchips/s). The range code was passed to the exciter, which phase-modulated it onto the carrier with a modulation index of 0.7 rad. For these tests, there was no command signal on the uplink. An uplink attenuator permitted the adjustment of the uplink signal-to-noise ratios (SNRs) before the uplink carrier passed into the Frontier Radio, which was in a separate screen room.

The downlink telemetry signal provided by the Frontier Radio is described by equation (21) of [2]. Parameters include the downlink carrier frequency, total signal power, peak modulation index ϕ_d, and telemetry waveform $\phi_{\mathrm{TM}}(t)$. The downlink carrier,

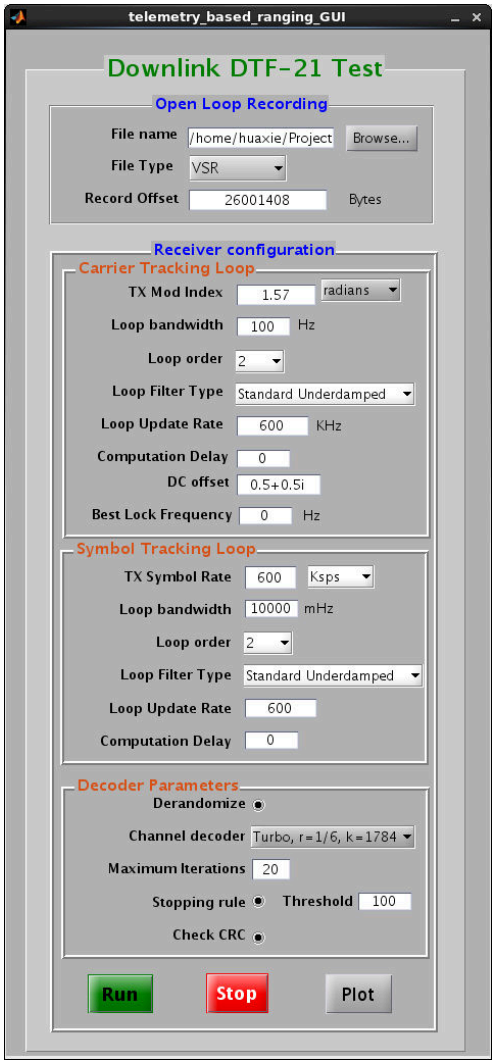

Figure 4. Graphical User Interface of the telemetry ranging software for processing test data.

with a frequency equal to 880/749 times the uplink carrier frequency, was modulated by telemetry using a modulation index of 1.21 rad. The downlink carrier was passed through a variable attenuator so that the downlink SNRs could be adjusted.

The telemetry ranging tests were conducted as part of a larger suite of performance verification and characterization testing of the Frontier Radio by the Deep Space Network (DSN) for the benefit of the Solar Probe Plus (SPP) mission. As such, the telemetry ranging test plan used the symbol rate and modulation index parameters planned for SPP. The parameters of the uplink and downlink signals used in the tests are summarized in Table 2.

Table 2. Transmission parameters used in tests.

	Parameter	Value(s)
Uplink		
	Carrier frequency (f_c)	7176.182859 MHz
	PN ranging type	DSN standard [6]
	Range clock frequency	$(221/(749 \cdot 2048)) \times f_c = 1.0338892$ MHz
	Range mod. index	0.7 rad
Downlink		
	Carrier frequency	$(880/749) f_c = 8431.296295$ MHz
	Mod. index	1.21 rad
	Channel code	(a) CCSDS (1784, 1/6) turbo code, (b) no coding
	Randomization	(a) On, (b) off
	Ranging	(a) Present on downlink, (b) not present
	Symbol rate	(a) 90.09014 ksps, (b) 600 ksps
	SNR	Variable

The downlink telemetry signal was a Consultative Committee for Space Data Systems (CCSDS) standard rate-1/6 turbo code [7]. The input to the encoder was a frame of 223 bytes, or 1784 bits, as shown in Figure 5. Most of the frame was a test pattern. Embedded in bit positions 128 through 159, however, was the Frontier Radio's range code phase measurement $\psi_{\mathrm{S}}(t_{\mathrm{S}})$, latched at the transmission time of the immediately preceding frame. The 20 bits in positions 128 to 147 (starting the counting at bit 0) contained the range code chip counter, an integer identifying a chip within the 1,009,470 chip period of the uplink PN range code. The 12 bits in positions 148 to 159 contained the fractional chip offset latched from the NCO. Bit 148 is 1/2 a chip, bit 149 is 1/4 chip, and so on. In this way, the 32 bits in positions 128 to 159 contain the integer and fractional part of the chip offset seen by the radio. The final two bytes of the information block were a 16-bit CRC, which can be used to validate correct decoding of the block. Each information block was randomized and then turbo encoded. Attached sync

markers (ASMs) are prepended to each codeblock, and the codewords were transmitted without gaps.

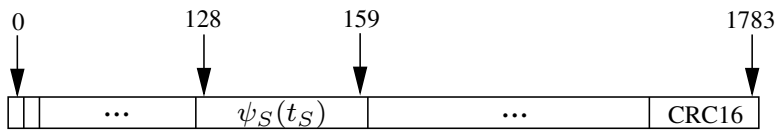

Figure 5. The format of the frame to be turbo-encoded.

A downconverter provided an IF carrier to an RSR, VSR, or PRSR. These open-loop receivers employed an external 100-MHz frequency reference and an external 1-PPS timing reference.

1. Incompleteness of the Test Data Collected

The essence of the algorithm to perform telemetry ranging is distilled from Eqs. (3), (4) and (5) of [1] or Eqs. (1) and (2) of [2]:

$$\int_{t_T}^{t_R} \dot{\psi}_T(t)dt = \psi_T(t_R) - \psi_S(t_S) \tag{1}$$

On the ground, one measures $\psi_T(t_R)$ at the estimated time of arrival t_R of a codeword bearing the range code phase $\psi_S(t_S)$ that was latched at the end of the uplink and inserted into the downlink telemetry. Decoding the codeword reveals the value of $\psi_S(t_S)$; note that the value of t_S remains unknown, but it is not needed. Then, to infer the time difference $t_R - t_T$ between the time of transmission t_T and the time of reception t_R of the telemetry ranging signal, one solves this equation for t_T from recordings of the ground phase $\psi_T(t)$ and its derivative $\dot{\psi}_T(t)$ over the interval $t \in [t_T, t_R]$.

For our tests at DTF-21, the ground phase $\psi_T(t)$ and its derivative $\dot{\psi}_T(t)$ were unfortunately not recorded, and thus these tests did not produce an explicit estimate of $t_R - t_T$. Nor did our tests include any calibration measurements to remove processing delays that would allow $t_R - t_T$ to be converted to the desired two-way geometric delay $\tau(t_R)$ for the two-way signal arriving on the downlink at time t_R. However, useful information about the inherent ranging errors on the uplink and the downlink can be inferred by examining the variability of the two quantities $\psi_S(t_S)$ and t_R that our tests did record (once per downlinked codeword). The next section analyzes the root mean square (rms) variabilities of $\psi_S(t_S)$ and t_R obtained from our test runs, and compares them to theoretical predictions developed in [2] of the rms errors in the uplink and downlink segments of the telemetry ranging system, and to the end-to-end performance analysis in Section III.

D. Analysis of the Test Data

We show an example of this type of analysis for a test begun at 0115UTC on day 262 (September 19). This test was conducted with rate–1/6 turbo-encoded downlink data at a symbol rate of 90 ksps. A total of 303 data blocks were recorded. Each data block was of approximately one second duration and comprised just over eight codewords, each codeword of length $(1784 + 4) \times 6$ symbols.

The measured symbol SNR E_s/N_0 of 11.7 dB was well above the threshold for successful turbo decoding, and all codewords decoded successfully. This resulted in a complete record of a total of 2498 observed values of the measured spacecraft phase $\psi_S(t_S)$ and the downlink arrival times t_R.

The raw range code phase samples exhibited a large deviation of the phase from its best linear fit, as shown in Figure 6. The raw rms error was 0.4957 chip. As seen in the

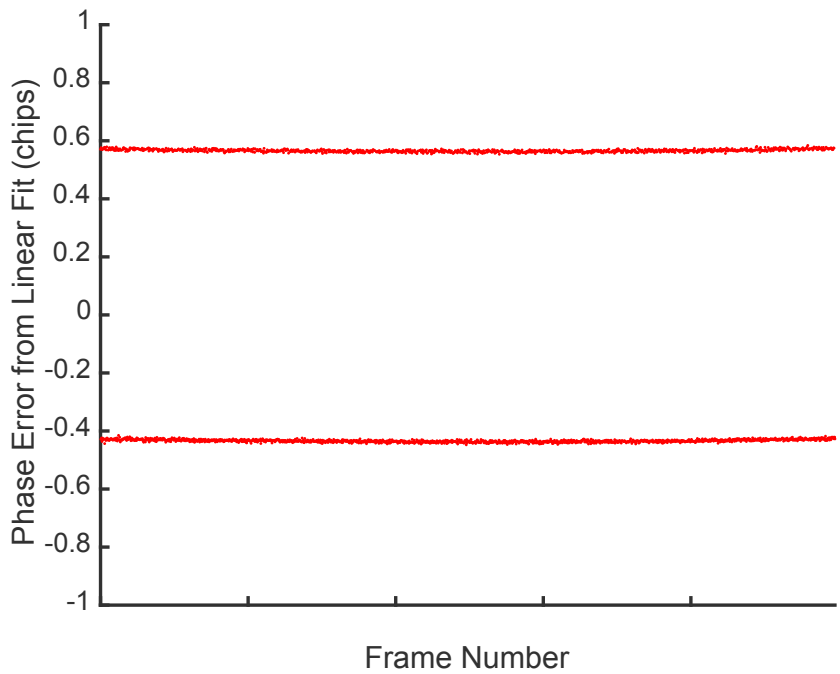

Figure 6. Raw uplink range code phase errors recorded for test 262-0115.

figure, the phase errors clustered into two distinct subsets separated by approximately one chip. The phases in these subsets are well fit by two different lines, and the overall best linear fit is not a good approximation to either set of phases.

This peculiar error in the phase $\psi_S(t_S)$ latched at the spacecraft was the result of a timing issue regarding the chip counter, and is easily correctable. This phase has two components, an integer chip count and a fraction. The fractional part is fine. The integer part is sometimes off by one unit, because the signal that tells the counter to increment has not been able to fully propagate through the chip counter at the time

that the spacecraft phase measurement is being latched. In particular, this means that some of the integer chip counts are correct, and some have a value is that is too low by exactly one chip.

After applying a simple software correction to identify and increment the too-low counts by one, the recorded phase data looks much better. The rms deviation is reduced to 0.0047 chip or 2.4 ns. Figure 7 shows a scatter diagram on a much expanded scale of the corrected range code phase error, together with the corresponding errors obtained after a 30-s smoothing of the corrected phases. The rms deviation of the smoothed data is 0.0031 chip or 1.6 ns, which is not much less than that of the corrected data without smoothing.

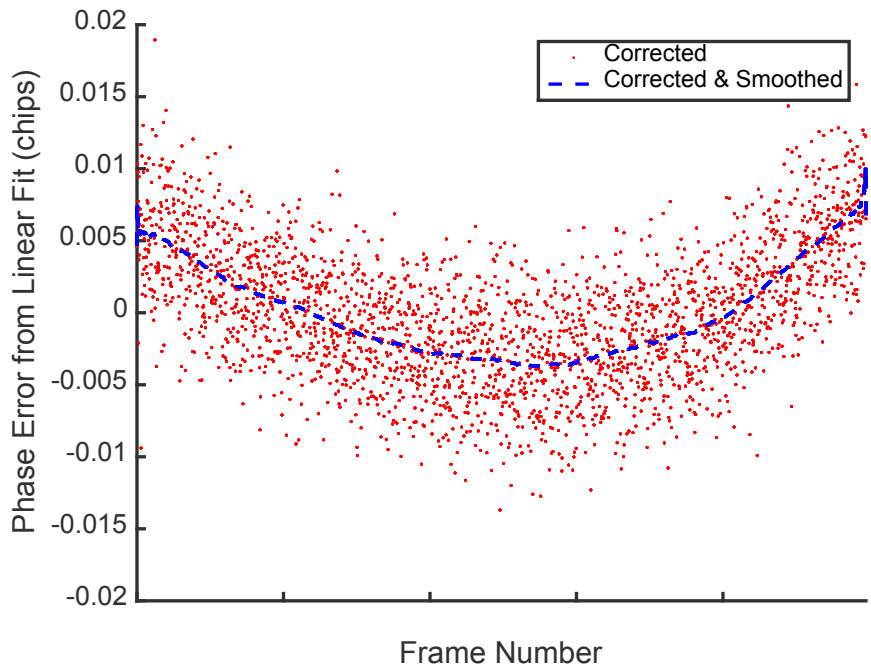

Figure 7. Corrected and smoothed corrected uplink range code phase errors recorded for test 262-0115.

Analysis of the frame arrival time data at the end of the downlink showed a much greater improvement from 30-s smoothing. Figure 8 shows a scatter diagram of the 2498 raw frame arrival times, together with the corresponding errors obtained after a 30-s smoothing of these arrival times. The rms deviations of the raw and smoothed timing data are 22.8 ns and 1.9 ns, respectively.

Figure 9 combines the results from Figures 7 and 8 to produce a scatter diagram of (unsmoothed) corrected phase errors versus 30-s smoothed frame arrival time errors, with both errors now measured in ns. Finally, a combined uplink and downlink timing error for each frame is estimated by root sum square (rss) combining the corrected uplink phase errors and smoothed downlink arrival time errors from the previous figure. This produces the scatter diagram of estimated end-to-end timing errors shown in Figure 10.

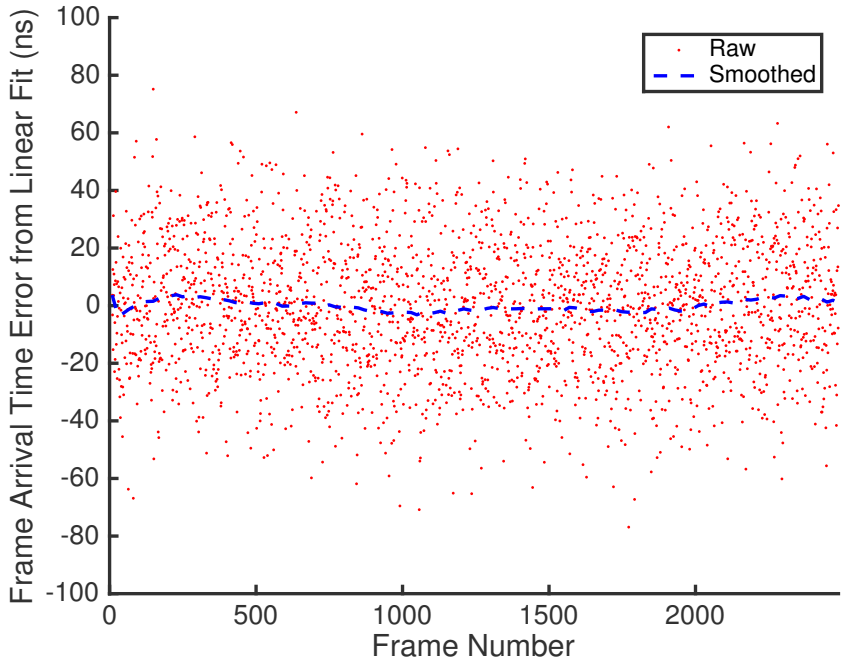

Figure 8. Raw and smoothed downlink frame arrival time errors recorded for test 262-0115.

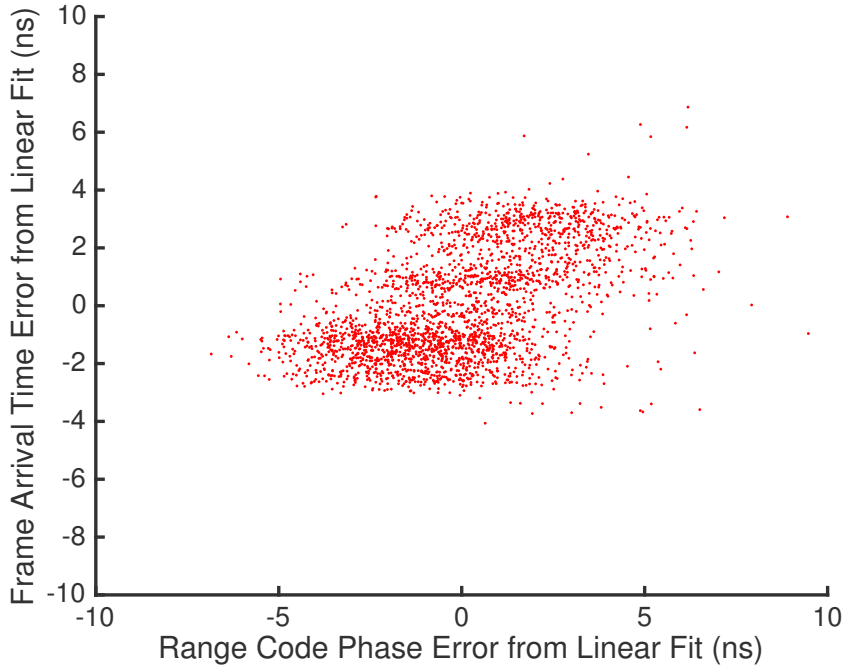

Figure 9. Scatter plot of corrected uplink phase errors and smoothed downlink arrival time errors recorded for test 262-0115.

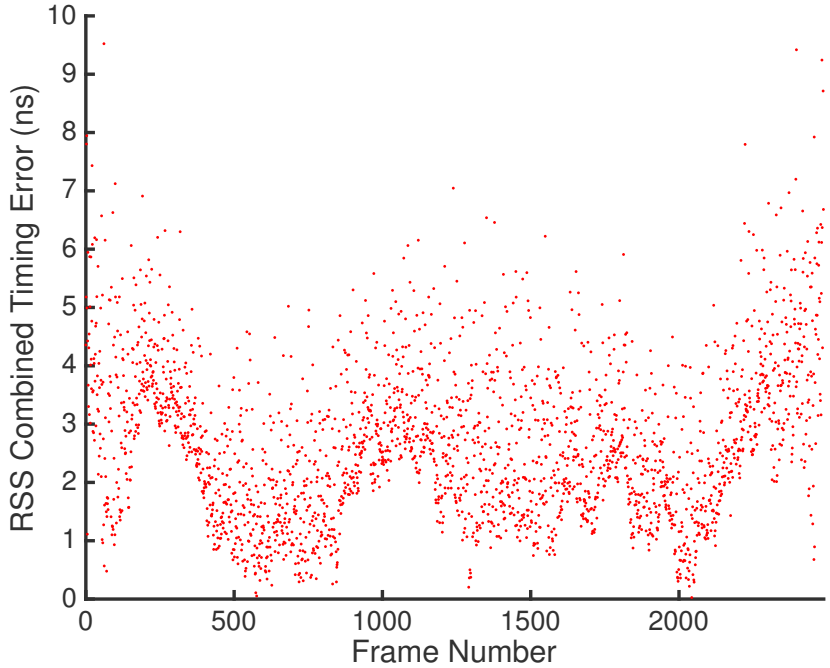

Figure 10. Scatter plot of rss-combined corrected phase and 30-s smoothed arrival time errors recorded for test 262-0115. Estimated rms combined timing error is 3.1 ns.

Similar results were obtained from additional test runs for which all of the codewords were successfully decoded. These test runs differed in the symbol rate, SNR, and whether an additional interfering regenerative ranging signal was transmitted on the downlink. Table 3 summarizes the parameter differences. Figure 11 and Figure 12 show the estimates of combined timing errors obtained from two test runs conducted at $E_s/N_0 = 12.56$ dB and $E_s/N_0 = 18.79$ dB, respectively.

Table 3. Parameters used in additional test runs.

Test run	Symbol rate (ksym/s)	b/sample	Sample rate (Msps)	Ranging on?	E_s/N_0
262-0115	90.09014	8	1	Yes	11.7
262-0126	90.09014	8	1	No	12.56
262-1655	90.09014	8	1	No	18.79
262-1745	600	2	4	Yes	5.95

We repeated this analysis for a test run at a considerably lower $E_s/N_0 = 5.95$ dB, for which all decoded frames passed their CRC checks but the turbo decoder indicated decoder failure for about 10% of frames. Figure 13 shows the estimated rms combined timing error obtained from analyzing only about the first 70% of decoded frames. As

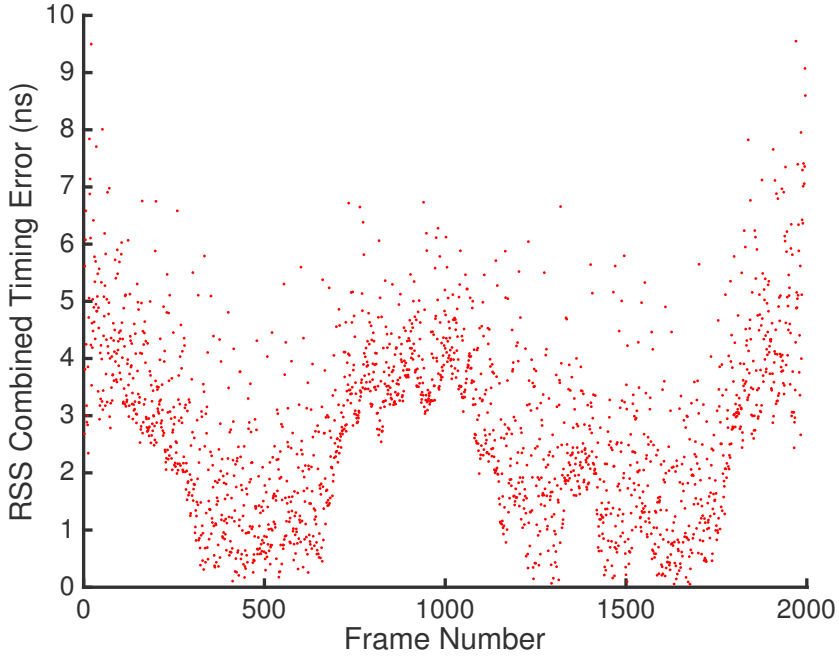

Figure 11. Scatter plot of rss-combined corrected phase and 30-s smoothed arrival time errors recorded for test 262-0126 conducted at $E_s/N_0 = 12.56$ dB. Estimated rms combined timing error is 3.4 ns.

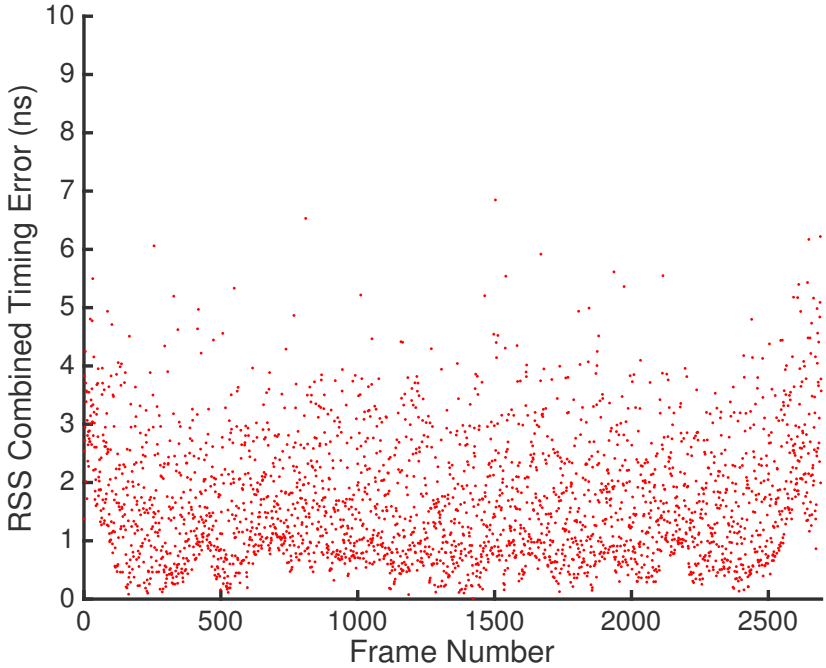

Figure 12. Scatter plot of rss-combined corrected phase and 30-s smoothed arrival time errors recorded for test 262-1655 conducted at $E_s/N_0 = 18.79$ dB. Estimated rms combined timing error is 2.1 ns.

in the other cases, the smoothing was applied over 250 frames, but this corresponds to a duration of only 4.5 s, since since the symbol rate was 600 ksps instead of 90 ksps.

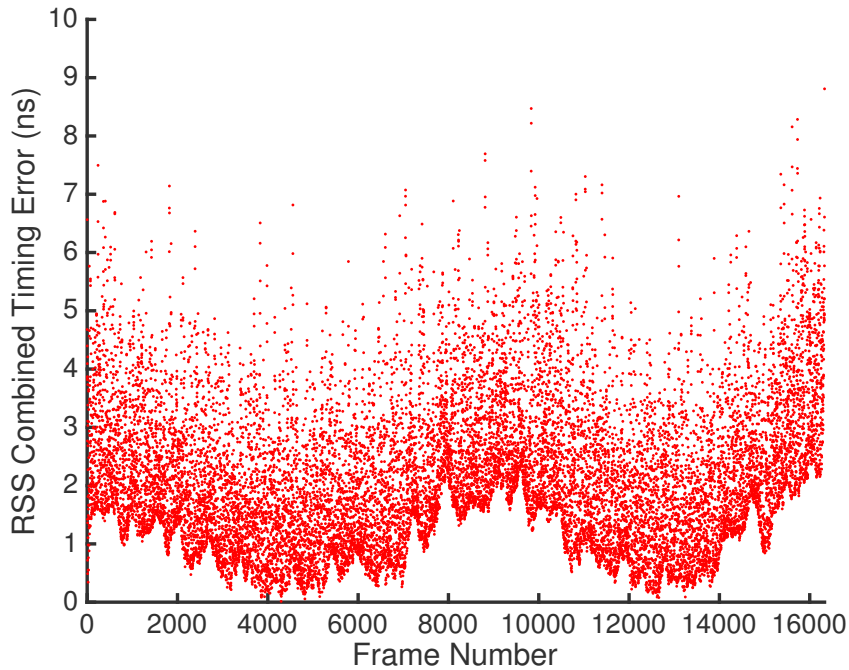

Figure 13. Scatter plot of rss-combined corrected phase and 4.5-s smoothed arrival time errors recorded for test 262-1745 conducted at $E_s/N_0 = 5.95$ dB. Estimated rms combined timing error is 2.5 ns.

Several other tests were excluded from the data reported here because the downlink telemetry stream failed to decode properly in its entirety. The causes of the telemetry failures were later determined to be related to human errors in configuring the sample rate or quantizer resolution of the open-loop recorders, accidental interference, dc bias, or other mis-configuration in the laboratory setup. No hardware issues in the DTF-21 hardware, Frontier Radio, or open-loop receivers were identified.

We examined the continuity of PN range-code phase between the following two data records: Test 262–1629 ("Record A") and Test 262–1655 ("Record B"). Record A started at 1629UTC on day 262, and Record B started approximately 26 minutes later at 1655UTC. For both of these records, the telemetry symbol rate was 90.09014 ksps, and the downlink sampling was at 1 MHz with 8 bits per sample. For Record A, E_s/N_0 was 13.85 dB and a regenerated ranging signal was present on the downlink (but was not examined in the post-processing). For Record B, E_s/N_0 was 18.79 dB and only telemetry was modulated onto the downlink carrier. For both records, the PN range-code phase, as conveyed in the telemetry frames, and the frame-arrival times were extracted and analyzed.

The Uplink Ranging Assembly was continuously generating the PN range code from the start of Record A through the end of Record B. The question of interest was whether we

could see continuity in the PN range-code phase in *post-processed* data from Records A and B.

There are two reasons why the *raw* PN range-code phase counts, as delivered by telemetry to the open-loop receiver, are not continuous. First, some phase counts from the Frontier Radio are too low by exactly one chip. (This issue is discussed above.) Second, the PN range-code phase, as it manifests itself in the range code, appears modulo $1,009,470$ chips (the period, in chips, of the composite range code).

For each of Records A and B, we were able, in post-processing, to correct both of these differences from the desired (unwrapped) phase continuity. The too-low by one chip anomaly was corrected as described earlier. Within Record A, the unwrapping of the PN range-code phase was accomplished by identifying and correcting each individual, abrupt loss of $1,009,470$ chips. The same was done for Record B.

When working with the two records together, there was the additional problem of identifying the loss of phase due to modulo arithmetic that occurs between the two records, when no data are available. The total loss of phase during this period must equal a positive integer times $1,009,470$ chips. By accounting for the time between the two records and the rate-of-change of phase, as determined by the linear fit of the unwrapped Record A phase, it was possible to identify the positive integer whose product with $1,009,470$ chips produces the phase loss due to modulo arithmetic within the silent period between the records.

With these corrections, the PN range-code phase of Record B looked like a linear extrapolation of the PN range-code phase of Record A, but with a pause (due to lack of data) in between. In order to better judge just how closely the Record B phases lie to the linear fit of the Record A phases, we removed the same linear fit, which was calculated from the Record A phases, from both Records A and B and then adjusted the arrival times so that the Record B phase errors (from the Record A linear fit) could be superimposed on the Record A phase errors. The result is shown in Figure 14. In making this figure, the Record B arrival times were decreased by 1582.5 s, relative to the Record A arrival times.

In Figure 14 the Record-A phase errors are shown in blue. The Record-B phase errors (from the Record A linear fit) are shown in green. In other words, the Record B data were adjusted by the trend determined for Record A, not by a linear fit to the Record B data. The vertical axis on the right side of Figure 14 makes this explicit.

As Figure 14 shows, the Record B phase errors cluster with the Record A phase errors. In fact, the Record B phase errors have a mean that is less than the Record A phase errors by 0.12 chip, which corresponds to a time delay of 6 ns. Thus, we conclude that for these two data records, having a common telemetry symbol rate, the phase continuity is good.

This demonstrated continuity of the phase in the PN range code between two records

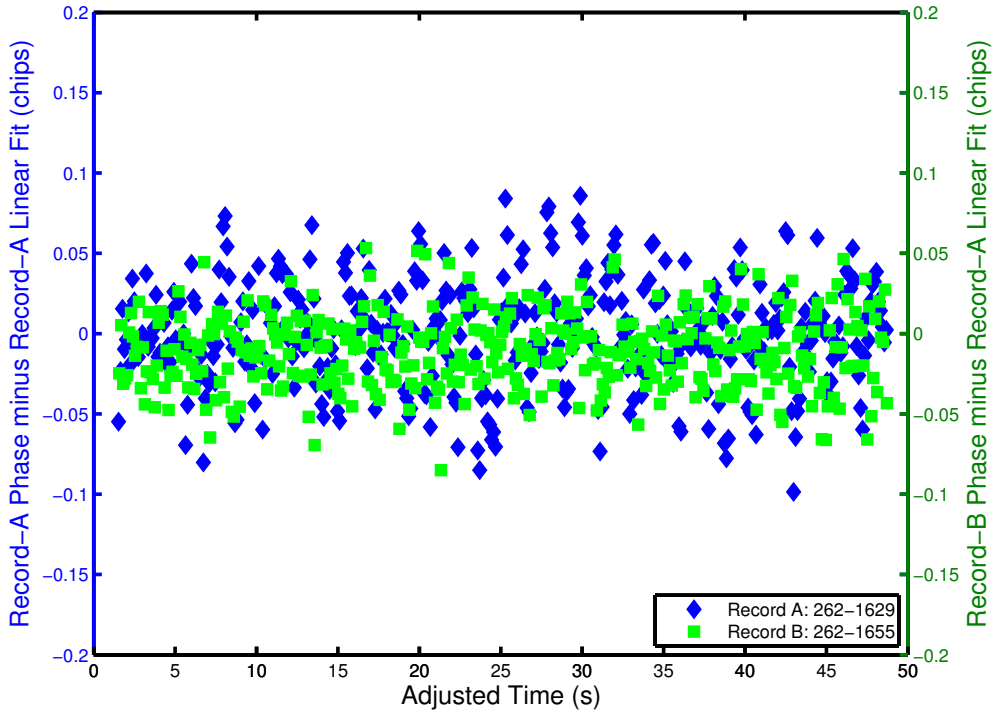

Figure 14. Phase errors for Records A and B, demonstrating phase continuity.

is what we expected to see, given that the PN range code was phase continuous at the Uplink Ranging Assembly. But the exercise was necessary, as we needed to confirm that there is no anomaly within the transponder that violates the phase continuity. The uplink carrier was modified between the two records, and the PN code-tracking loop in the Frontier Radio was interrupted between the two records and then relocked. Despite this interruption within the transponder, the phase continuity of the Uplink Ranging Assembly flowed to the PN range-code phase samples conveyed by telemetry, to within 6 ns.

E. Lessons Learned from the Initial Analysis

During the processing of data records having only 2 bits per sample, an anomalous effect was observed. When post-processing the IF carrier using a software receiver, an unexpected oscillation appeared in the phase of the carrier loop's NCO.

The expectation had been that the NCO phase would track the phase of the IF carrier. But there was no counterpart of the NCO phase oscillation in the IF carrier. Therefore, the NCO phase oscillation was regarded as anomalous.

After analysis and simulation were brought to bear on this issue, the NCO phase oscillation was eventually explained. In the process, we learned how, in the future, to preclude this problem. Following is an analytical explanation for the origin of the NCO

phase oscillation and a recommendation for avoiding this problem in the future.

During the laboratory tests, the final IF, at the input to the carrier-tracking loop, was a very small frequency. Since complex samples were used, that final IF could even have been 0 Hz without introducing an aliasing problem. In our case, the receiver local oscillators were not coherently related to the uplink carrier, so the final IF was small, but not exactly 0 Hz.

For those records having only 2 bits per sample, there was a dc bias that arose because the discrete set of possible complex samples were not symmetrically positioned about 0. It was this dc bias that gave rise to the NCO phase oscillation. The analysis below demonstrates this fact.

We model a carrier plus dc bias in discrete time as

$$x(n) = c + \sin(\omega n). \tag{2}$$

For the sake of convenience, the carrier is modeled as having an amplitude of 1. The constant c is the ratio of the dc bias to the amplitude of the carrier. The discrete-time index is n. The phase of the carrier advances by ω radians from one sample to the next

A mathematically equivalent expression for $x(n)$ is

$$x(n) = A\sin(\omega n + \theta), \tag{3}$$

where

$$A = \sqrt{c^2\cos^2(\omega n) + [1 + c\sin(\omega n)]^2}, \tag{4}$$

and

$$\theta = \tan^{-1}\left[\frac{c\cos(\omega n)}{1 + c\sin(\omega n)}\right]. \tag{5}$$

When the dc bias is very small compared with the carrier's amplitude, we may use $|c| \ll 1$ to find a simpler, approximate expressions for A and θ:

$$A \approx 1 + c\sin(\omega n) \tag{6}$$

$$\theta \approx c\cos(\omega n). \tag{7}$$

Each of the above approximations employs the first two terms in a Maclaurin series expansion when considering $|c| \ll 1$. If we use both of these approximations, we get the following approximate expression for $x(n)$:

$$x(n) \approx [1 + c\sin(\omega n)]\sin(\omega n + c\cos(\omega n)). \tag{8}$$

Let us consider what happens when tracking this signal with a digital phase-locked loop (DPLL). There is both amplitude modulation and phase modulation present on the signal. Automatic gain control (AGC) might remove the amplitude modulation; even if this is not the case, however, the loop will be less sensitive to amplitude modulation than

to phase modulation. Therefore, in a first-order analysis, we will ignore the amplitude modulation.

In the approximation $|c| \ll 1$, a sinusoid modulates the phase of the carrier. The modulating sinusoid, $c\cos(\omega n)$, has a frequency equal to the carrier frequency. In this analysis, we assume that the loop bandwidth for this DPLL is larger than $\omega/(2\pi T_s)$ Hz, where T_s is the sample period in seconds. (If this is not the case, than the DPLL won't see the entire $x(n)$ and this analysis is unnecessary.) With the DPLL loop bandwidth larger than $\omega/(2\pi T_s)$, the DPLL will track the phase modulation. The NCO will produce a signal that is approximately of the form

$$\text{NCO output} = \cos(\omega n + c\cos(\omega n)). \tag{9}$$

The NCO phase will therefore contain a linear ramp in time (ωn, which tracks the IF carrier), and there is a sinusoidal variation, $c\cos(\omega n)$, superimposed on the ramp.

The situation may be summarized as follows. The final IF carrier frequency was very small and the dc bias fell within the DPLL bandwidth. In essence, then, the dc bias looked like an interfering signal to the loop.

The sinusoidal variation appearing in the NCO phase can be precluded by using a DPLL loop bandwidth that is less than $\omega/(2\pi T_s)$. Of course, when using a narrow loop bandwidth, it might be necessary to adjust the best-lock frequency of the DPLL to equal the expected frequency of the carrier. This can be done with a well-chosen additive constant in the frequency register of the DPLL.

It would be advantageous in future DTF-21 tests to use a larger final carrier IF. For example, if a final carrier IF of about 100 Hz is selected, then the carrier is farther away from the dc bias. This will improve the operation of the software DPLL if the best-lock frequency can be adjusted to the final carrier IF (100 Hz in this example) and if the DPLL loop bandwidth is reduced so that the dc bias falls outside the loop bandwidth.

III. End-to-End Ranging Accuracy

In this section, we analyze the performance of an ideal telemetry ranging system, including the effects of carrier tracking errors on PN code phase and codeword delay measurement.

We assume residual carrier modulation with a rectangular pulse shape is used on both the uplink and downlink. The uplink and downlink signals are received using the signal processing described in Figures 14 and 15, respectively, of [2]. Briefly, for the uplink this includes a DPLL to recover the uplink carrier phase, and another DPLL (which we designate as the PN-DPLL, to distinguish it) to track the range code of the PN waveform. For the downlink, the processing includes a DPLL to recover the downlink carrier phase, and a data-transition tracking loop (DTTL) to recover the symbol timing.

A. Mathematical Model for Determining Telemetry Ranging End-to-End Performance

The theoretical performance of the end-to-end telemetry ranging system is determined by evaluating the Cramér-Rao bound (CRB) on symbol and chip synchronization, taking into account the degradation caused by phase errors in the carrier tracking system. First, a useful model of the phase errors in the carrier tracking loops is developed, for residual carrier modulation. Next, a model for the "average effective power" of the signal in the PN tracking loop is developed, and applied to the CRB for chip or symbol synchronization to obtain the average CRB characterizing the cascade in both the spacecraft and ground receivers. Since the errors in the spacecraft and on the ground are independent, the variance of the total two-way delay error can be calculated by adding the variance of the delay errors on the spacecraft and at the ground receiver. In this theoretical development, we can equivalently add the average CRB of the ground and spacecraft receivers, because the averaged CRBs are lower bounds on the delay error variance and hence add for independent processes. We begin by developing useful models for the probability density of phase error in residual carrier phase-locked loops.

1. Probability Density of Phase Error in Residual Carrier Receivers

The Tikhonov density accurately models the probability density of the phase error $\Delta\theta$ in a PLL [8], over the range $-\pi < \Delta\theta < \pi$. The Tikhonov density is given by the expression

$$p(\Delta\theta) = \frac{\exp[\rho\cos(\Delta\theta)]}{2\pi I_0(\rho)}, \tag{10}$$

where, as in Eq. (116) of [2], $\rho = P_c/(N_0 B_L)$ is the "loop SNR." Here P_c is the residual carrier power of the signal, N_0 is the spectral level of the complex noise, B_L is the loop bandwidth, and $I_0(\rho)$ is the modified Bessel function of the first kind with argument ρ. As described in (40) of [2], P_c is related to total signal power P_t by $P_c = P_t\cos^2(\phi_r)$, where ϕ_r is the modulation index used to partition signal power between the residual carrier and the data modulation.

The expression in (10) is numerically difficult to compute for $\rho > 100$, because MATLAB returns "Inf" for both $\exp(\rho)$ and $I_0(\rho)$. To overcome this problem, we can make use of the following asymptotic expression for the modified Bessel function of the first kind:

$$I_0(\rho) = \frac{\exp(\rho)}{\sqrt{2\pi\rho}}\left(1 + \frac{1}{8\rho} + \frac{9}{2!(8\rho)^2} + o(\rho^{-2})\right) \overset{\rho\gg 1}{\approx} \frac{\exp(\rho)}{\sqrt{2\pi\rho}}. \tag{11}$$

We may also expand the cosine term as

$$\cos(\Delta\theta) = 1 - \frac{(\Delta\theta)^2}{2!} + \frac{(\Delta\theta)^4)}{4!} - \cdots \overset{|\Delta\theta|\ll 1}{\approx} 1 - \frac{(\Delta\theta)^2}{2}, \tag{12}$$

where we have assumed that for large loop SNR the phase error is small. Substituting (11) and (12) into (10) yields the following large SNR approximation of the Tikhonov density:

$$p(\Delta\theta) = \frac{\exp[\rho\cos(\Delta\theta)]}{2\pi I_0(\rho)} \overset{\rho\gg 1,\ |\Delta\theta|\ll 1}{\approx} \frac{\exp(\rho)\exp[-\rho(\Delta\theta)^2/2]}{2\pi\exp(\rho)/\sqrt{2\pi\rho}} = \frac{\exp[-\rho(\Delta\theta)^2/2]}{\sqrt{2\pi/\rho}}. \tag{13}$$

This is recognized as a Gaussian density for the phase error $\Delta\theta$, with zero mean and variance $1/\rho$. An example of the true Tikhonov density and its large-ρ Gaussian approximation is shown in Figure 15, for the case $\rho = 5$ dB. Note the good agreement

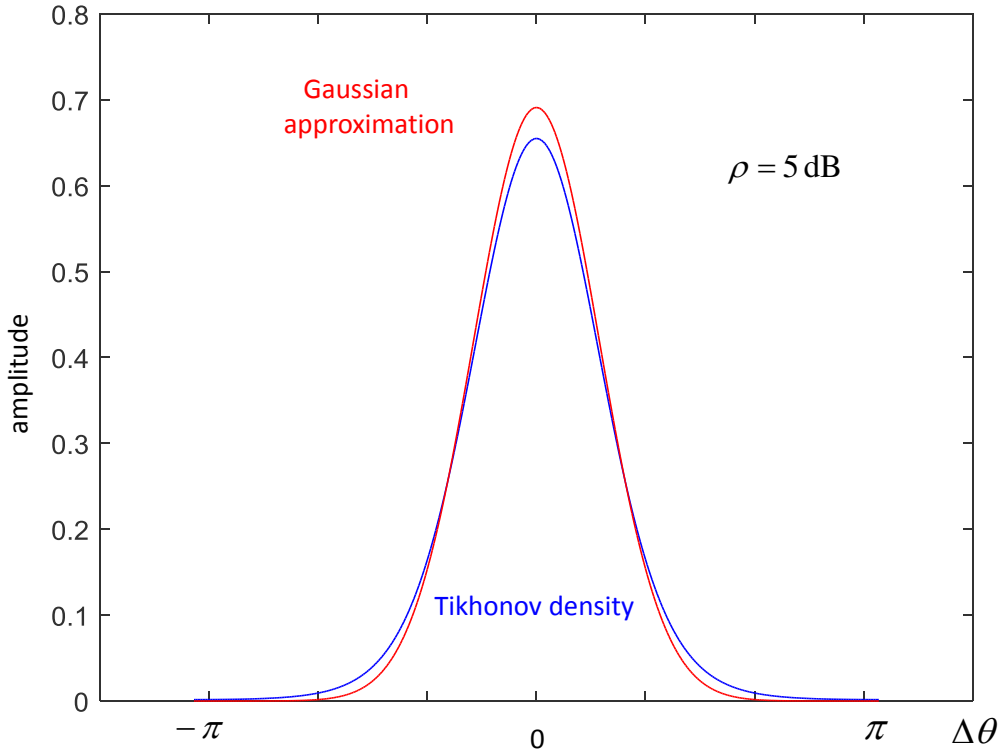

Figure 15. Comparison of Tikhonov density (blue curve) and its high-SNR Gaussian approximation (red curve) for the case $\rho = 5$ dB.

between the Tikhonov density and its simpler Gaussian approximation, even for the relatively modest loop SNR of $\rho = 5$ dB: the approximation improves at higher SNR, to the point where the two curves are virtually indistinguishable for $\rho > 20$ dB. However, the Gaussian approximation extends over the range $-\infty < \Delta\theta < \infty$ and therefore represents an "unwrapped" phase, whereas the Tikhonov density is restricted to the range $\pi < \Delta\theta < \pi$, which better describes the response for typical communications and ranging equipment, such as PLLs.

2. Uplink Receiver: Averaged Power CRB for Residual Carrier Signals

As shown in [8], the CRB for estimating the phase of a square-wave-like compound PN code is given by the expression

$$\mathrm{var}(\Delta\varphi) \geq \frac{\pi^2 N_0 B_L}{8 P_t \sin^2(\phi_r)} = \frac{\pi^2 N_0 B_L}{8 P_r} \quad \mathrm{rad}^2, \tag{14}$$

where as in (41) of [2], $P_r = P_t \sin^2(\phi_r)$ is the portion of the total power allocated to the PN modulation. If the carrier-tracking DPLL preceding the PN-DPLL main-

tains a constant but small phase offset $\pi/2 > |\Delta\theta| > 0$, the power allocated to the the PN-DPLL is reduced by the factor $\cos^2(\Delta\theta)$, yielding reduced power $P_r(\Delta\theta) = P_t \sin^2(\phi_r)\cos^2(\Delta\theta) = P_r \cos^2(\Delta\theta)$, and resulting in degraded PN-DPLL performance. In this case, the CRB for the PN-DPLL becomes $\mathrm{var}(\Delta\varphi|\Delta\theta) \geq \pi^2 N_0 B_L/(8P_r(\Delta\theta))$.

The PN-DPLL acquires the complex baseband carrier by adjusting the phase of the local oscillator (or NCO in a digital implementation) to be $\pi/2$ radians out of phase with the received carrier. A difference of $\Delta\varphi$ between the phase of the compound PN codeword (here treated as a simple sinusoid) and the phase of the NCO tracking the PN code phase, generates an error signal $\epsilon(\Delta\varphi|\Delta\theta)$ proportional to $\Delta\varphi$, with amplitude $\sqrt{P_r}\cos(\Delta\theta)$:

$$\epsilon(\Delta\varphi|\Delta\theta) = \sqrt{P_r}\cos(\Delta\theta)\sin(\Delta\varphi) \overset{|\Delta\varphi|\ll\pi/2}{\approx} \sqrt{P_r}\cos(\Delta\theta)\Delta\varphi. \tag{15}$$

Under nominal operating conditions, the phase error in the residual carrier tracking loop (DPLL) is small, $\Delta\theta \ll 1$, hence the amplitude of the error signal is approximately $\sqrt{P_r}$, yielding the following approximate expression for the error signal: $\epsilon(\Delta\varphi|\Delta\theta \ll \pi/2) \approx \sqrt{P_r}\Delta\varphi$. Assuming the ranging power is known (or can be estimated accurately) the error signal is normalized and the resulting phase error $\Delta\varphi$ applied to the NCO, driving the error signal towards zero in the absence of noise and phase dynamics. However, if the residual carrier phase error exceeds $\pi/2$ radians, the sign of the amplitude changes, yielding the negative of the true error signal and hence generating an error signal that drives the NCO in the wrong direction.

If the phase error is not a constant offset but a time-varying process $\Delta\theta(t)$, then the definition of the average "effective power" within the PN-DPLL must be re-examined. The following development is based on the observation that above threshold, the performance of an ideal PLL follows the CRB closely, hence it provides a structure for interpreting the meaning of "effective power" in the context of PLLs that can be applied to the CRB of the cascaded system.

Consider the case where the PN-DPLL is operating with a loop bandwidth of B_{PN}, where the loop is effectively averaging the error signal over a time-interval corresponding to the coherence-time of the loop, namely $T_{PN} = 1/(2B_{PN})$. If the bandwidth of the DPLL is $B_{rc} > B_{PN}$, the number of independent carrier phase-error samples in a PN tracking loop (PN-DPLL) coherence time T_{PN} is $N_{PN} = 2B_{rc}T_{PN} = B_{rc}/B_{PN}$. The time-varying phase error process $\Delta\theta(t)$ can be expanded over a T_{PN}-second time interval in terms of orthonormal sampling functions $\psi_i(t)$ as $\Delta\theta(t) = \sum_i \Delta\theta_i\psi_i(t)$, where $\Delta\theta_i = \int \Delta\theta\psi_i(t)\,dt$. Each independent sample is a random variable, taking on the value $\Delta\theta_i, 1 < i \leq N_{PN}$ with probability density $p(\Delta\theta_i)$. In the PN tracking loop, the error signal is effectively integrated over the coherence-time of the tracking loop. For the case of a large phase error that exceeds $\pi/2$ radians, the error signal becomes negative, and hence cancels out a corresponding error signal sample with the same (or similar) amplitude. Therefore, the total number of samples contributing to the average error signal is reduced by two samples, from N_{PN} to $N_{PN} - 2$. For a large number of samples, this corresponds to the case where the probability that $\Delta\theta > \pi/2$

is approximately $1/N_{PN}$, or equivalently $\Pr[\Delta\theta > \pi/2] = 2\int_{\pi/2}^{\pi} p(\Delta\theta)\, d\Delta\theta$. In general, negative amplitudes cancel an equal number of positive amplitudes, hence the effective average number of samples that contribute to the error signal in a loop coherence time is proportional to the average positive amplitudes minus the average negative amplitudes.

The average value of the positive signal amplitude is

$$\overline{\sqrt{P_r^+}} = \sqrt{P_r} \int_{-\pi/2}^{\pi/2} \cos(\Delta\theta) p(\Delta\theta)\, d\Delta\theta, \tag{16}$$

whereas the average negative signal amplitude is

$$\overline{\sqrt{P_r^-}} = 2\sqrt{P_r} \int_{\pi/2}^{\pi} \cos(\Delta\theta) p(\Delta\theta)\, d\Delta\theta. \tag{17}$$

Therefore, it is reasonable to define the average effective amplitude as

$$\overline{\sqrt{P_{eff}}} = \overline{\sqrt{P_r^+}} - \overline{\sqrt{P_r^-}}, \tag{18}$$

and hence the average effective power as

$$\overline{P_{eff}} = \left(\overline{\sqrt{P_r^+}} - \overline{\sqrt{P_r^-}}\right)^2. \tag{19}$$

Since this represents the effective signal power that generates the error signal, it is reasonable to use this effective power when a large number of independent samples are averaged in a tracking loop.

The average effective power can be used to compute the variance of the phase error of the cascaded carrier DPLL PN-DPLL system, via the analogy between the theoretical CRB and the structured tracking loops whose performance converges to the CRB, above threshold. Substituting the average effective power into the expression for the variance of the PN-DPLL phase error, when the effect of the random phase error input from the preceding DPLL stage is taken into account, yields the following expression for the performance of the cascaded system:

$$\mathrm{var}(\Delta\varphi) \geq \frac{\pi^2}{8} B_L / \left(\overline{P_{eff}}/N_0\right) = \frac{\pi^2}{8} N_0 B_L \left(\overline{\sqrt{P_r^+}} - \overline{\sqrt{P_r^-}}\right)^{-2}, \tag{20}$$

where $\overline{\sqrt{P_r^+}} = \sqrt{P_r}\int_{-\pi/2}^{\pi/2} \cos(\Delta\theta) p(\Delta\theta)\, d\Delta\theta$, $\overline{\sqrt{P_r^-}} = 2\sqrt{P_r}\int_{\pi/2}^{\pi} \cos(\Delta\theta) p(\Delta\theta)\, d\Delta\theta$, and $P_r = P_t \sin^2(\phi_r)$. The theoretical performance of the cascaded DPLL PN-DPLL system is shown in Figure 16 as a function of P_t/N_0, together with the "stand-alone" performance of the PN-DPLL, for the case $B_{rc} = 100$ Hz, $B_{PN} = 1$ Hz, and $\phi_r = 0.4\pi$. Note that above $P_t/N_0 > 45$ dB-Hz , the phase error $\Delta\theta$ is so small that the PN signal amplitude doesn't degrade appreciably, and the average value of the negative amplitude signals is negligible. However, below $P_t/N_0 < 40$ dB-Hz the DPLL phase errors become large enough to reduce the effective signal power, leading to a notable increase in the cascaded phase error variance. As the DPLL SNR decreases further, 2π radian cycle-slips begin to occur in the carrier tracking loop leading to narrow spikes in the phase

error, however the PN-DPLL flywheels through the spikes due to its narrower loop bandwidth, and continues to track the PN code down to about 30 dB-Hz, below which rapid degradation occurs and the cascaded system stops tracking at the threshold value of $P_t/N_0 \approx 28$ dB-Hz, as evident in Figure 16. The theoretical results for the averaged power are validated by MATLAB simulation of the cascaded system, as described in [2]. Red circles are the simulation results for the stand-alone PN-DPLL, while the blue circles are simulation results for the cascaded DPLL PN-DPLL system.

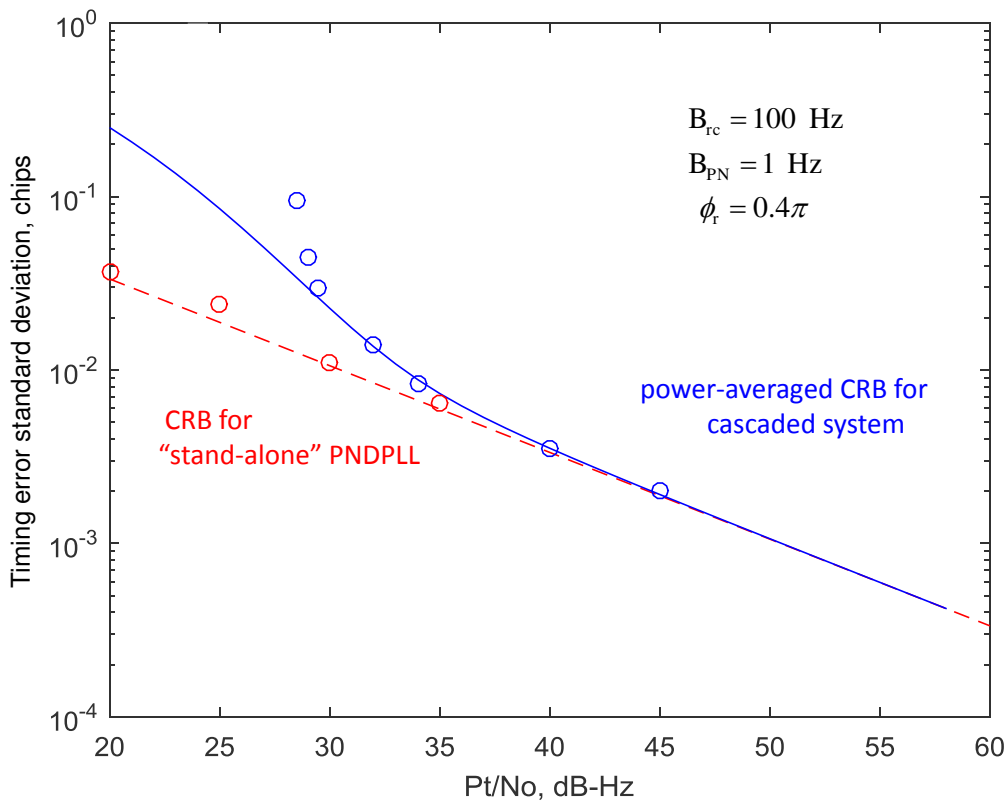

Figure 16. Comparison of "stand-alone" PN-DPLL performance (CRB dashed red line, simulation red circles), with "power-averaged" cascaded system (power-averaged CRB solid blue line, simulation blue circles).

3. Downlink Receiver: Averaged Power CRB for Residual Carrier Signals

The average effective power concept developed above can also be applied to the downlink, when the downlink modulation index is less than $\pi/2$ radians, hence a residual carrier is available for DPLL tracking. However, a major difference between the uplink and downlink channels is that the modulation on the uplink carrier uses a known compound PN code that resembles a square wave and hence can be tracked with a modified PLL, whereas the modulation on the downlink channel is random data that cannot be tracked with a PLL, requiring instead a dedicated symbol synchronization system such as a DTTL. Following carrier phase tracking via DPLL, the quadrature component of

the signal containing the random data modulation is input to a DTTL to establish symbol synchronization. When the carrier phase is tracked with a DPLL, the phase error entering the DTTL is again characterized by the Tikhonov density of (10).

Since the DTTL multiplies a noisy transition estimate with a noisy error estimate, a squaring loss S_L will be observed when the transition estimates are degraded by noise. Windowing is often used in DTTL applications to improve noise performance, since a fractional symbol window of $W = 2^{-n}$, $n = 0, 1, 2, \ldots$, applied to mid-phase integration effectively reduces the noise power by a factor of W, thus improving the delay-error performance of the DTTL by a corresponding amount.

The squaring loss for the DTTL, S_L, is given by [9]

$$S_L = \frac{\left[\operatorname{erf}\left(\sqrt{R_s}\right) - \frac{W}{2}\sqrt{\frac{R_s}{\pi}}\exp(-R_s)\right]^2}{\left\{1 + \frac{WR_s}{2} - \frac{W}{2}\left[\frac{1}{\sqrt{\pi}}\exp(-R_s) + \sqrt{R_s}\operatorname{erf}\left(\sqrt{R_s}\right)\right]^2\right\}} \tag{21}$$

where $R_s = P_d T_s / N_0$, and T_s is the symbol duration in seconds. Taking both windowing and squaring loss into account, the CRB for the fractional delay error $\Delta\tau$ expressed in terms of symbol durations becomes

$$\operatorname{var}(\Delta\tau) \geq \frac{WB_L}{2S_L P_d/N_0} \quad \text{sym}^2 \tag{22}$$

where S_L is defined in (21). In the high-SNR limit the transition estimates are essentially noise-free hence there is no squaring-loss, $S_L \to 1$, and the CRB for the DTTL can be expressed as

$$\operatorname{var}(\Delta\tau) \geq \frac{WB_L}{2P_d/N_0} \quad \text{sym}^2. \tag{23}$$

To obtain the low-SNR limit, $R_s \ll 1$, we use the following small-argument approximiations: $\operatorname{erf}(\sqrt{R_s}) \approx 2\sqrt{R_s/\pi}$, $\sqrt{R_s}\operatorname{erf}(\sqrt{R_s}) \approx 2R_s/\sqrt{\pi}$, $\exp(-R_s) \approx 1 - R_s$. Substituting into (21) and simplifying yields

$$S_L \overset{R_s \ll 1}{\approx} \frac{4R_s}{\pi}\left[1 - \frac{W}{4}\right]^2\left[1 - \frac{W}{2\pi}\right]^{-1} = \alpha(W)R_s, \tag{24}$$

where $\alpha(W) = \frac{4}{\pi}\left[1 - \frac{W}{4}\right]^2\left[1 - \frac{W}{2\pi}\right]^{-1}$. Applying the above approximation for S_L and letting $R_s = P_d T_s / N_0$, the low-SNR CRB becomes

$$\operatorname{var}(\Delta\tau) \geq \frac{WB_L}{2\alpha(W)R_s(P_d/N_0)} = \frac{WB_L}{2\alpha(W)T_s(P_d/N_0)^2} \quad \text{sym}^2. \tag{25}$$

In the presence of residual phase error process $\Delta\theta(t)$ from the DPLL, the data power P_d is again replaced by the average effective data power $\overline{P_{eff}} = \left(\overline{\sqrt{P_d^+}} - \overline{\sqrt{P_d^-}}\right)^2$, yielding the following approximations to the high-SNR and low-SNR CRB for the cascaded DPLL-DTTL system, when the ratio of DPLL to DTTL bandwidths are large:

$$\text{high-SNR:} \quad \operatorname{var}(\Delta\tau) \geq \frac{WN_0B_L}{2}\left(\overline{\sqrt{P_d^+}} - \overline{\sqrt{P_d^-}}\right)^{-2} \quad \text{sym}^2 \tag{26}$$

$$\text{low-SNR:} \quad \operatorname{var}(\Delta\tau) \geq \frac{WN_0^2B_L}{2\alpha(W)T_s}\left(\overline{\sqrt{P_d^+}} - \overline{\sqrt{P_d^-}}\right)^{-4} \quad \text{sym}^2 \tag{27}$$

The delay-error performance of the DTTL as a function of P_t/N_0 is shown in Figure 17, for the case of 1-MHz data symbol rate, modulation index $\phi_d = 0.4\pi$, closed-loop DTTL bandwidth $B_L = 1$ Hz and DPLL bandwidth of $B_L = 100$ Hz. It can be seen that the low-SNR and high-SNR CRB models cross above 60 dB-Hz in Figure 17, but may change significantly for a different choice of parameters.

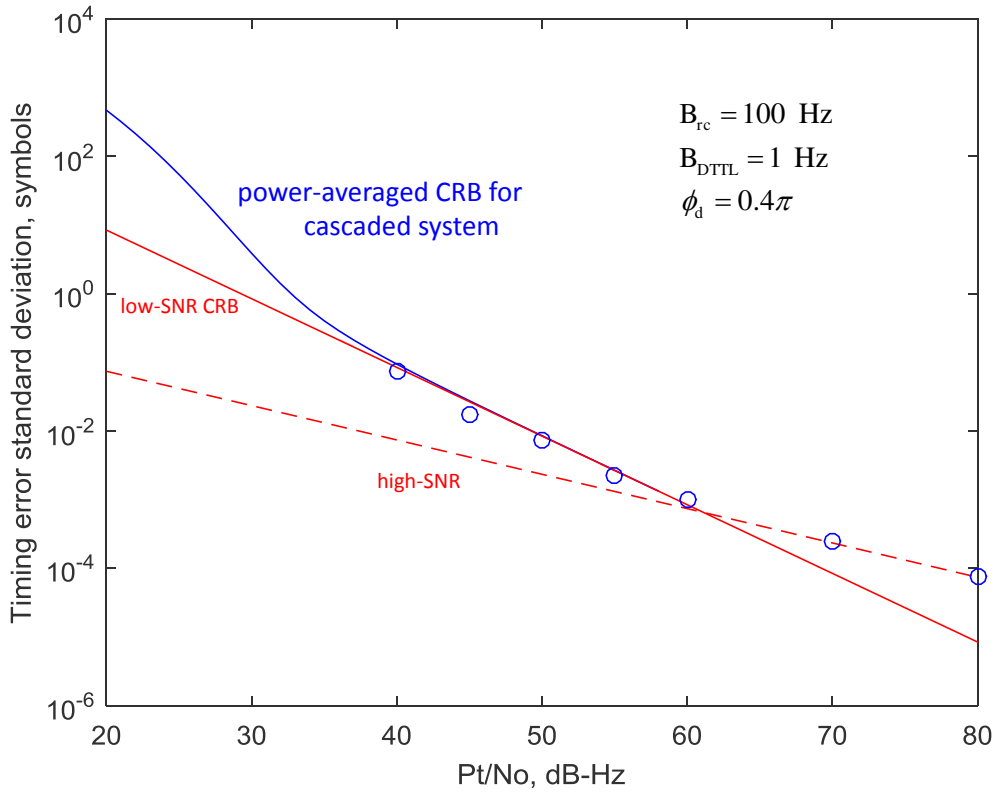

Figure 17. Cascaded DPLL DTTL performance, for residual carrier with random data modulation, with BPSK data, $T_s = 10^{-6}$ s and $W = 1$. Blue circles are simulation results.

4. End-to-End Range Error Model

The phase and delay error variances developed above for the uplink and downlink can be re-expressed in common units of squared distance. On the uplink, two chips of the range clock corresponds to a cycle of 2π radians, and so (14) may be rewritten as

$$\mathrm{var}(\Delta\varphi) \geq \frac{B_L N_0}{8P_r} \quad \mathrm{chip}^2. \tag{28}$$

This CRB does not include a loss factor to account for the occasional sign-flips in the compound PN code: for the T4B code, the loss factor is approximately 0.9, which can be included in the theoretical CRB for more accurate results. In terms of fractional chips, using the simplified notation σ^2_{PN} for the variance of the fractional chip error,

the power-averaged CRB for the cascaded carrier tracking DPLL and PN-code tracking PN-DPLL can be expressed as

$$\sigma_{PN}^2 = \frac{B_L N_0}{8\overline{P_{eff}}} = \frac{B_L N_0}{8}\left(\overline{\sqrt{P_r^+}} - \overline{\sqrt{P_r^-}}\right)^{-2} \quad \text{chip}^2. \tag{29}$$

Chips of duration T_c s can be converted to two-way range (m) by recognizing that a T_c s delay corresponds to cT_c m of range in a vacuum, where $c = 2.99792458 \times 10^8$ m/s. Applying the conversion factor cT_c m/chip yields

$$\sigma_{PN}^2 = \frac{1}{8}c^2 T_c^2 N_0 B_L \left(\overline{\sqrt{P_r^+}} - \overline{\sqrt{P_r^-}}\right)^{-2} \quad \text{m}^2 \tag{30}$$

as the variance of the cascaded DPLL PN-DPLL system, in terms of range error. For example, for $T_c = 0.5 \times 10^{-6}$ s, $cT_c = 0.5 \times (2.99792458 \times 10^2) \approx 150$ m.

The same approach can be used to convert the delay error of the cascaded DPLL DTTL system used in the ground receiver, expressed in terms of fractional symbol (or chip) error. Using the conversion factor cT_s m/sym, the variance of the cascaded ground receiver system is

$$\sigma_d^2 \geq \frac{c^2 T_s^2 W B_L}{2S_L \overline{P_{eff}}/N_0} \quad \text{m}^2 \tag{31}$$

where S_L is given by (21). The corresponding high and low SNR limits on two-way range variance are

$$\text{high-SNR:} \quad \sigma_d^2 \geq \frac{c^2 {T_s}^2 W N_0 B_L}{2}\left(\overline{\sqrt{P_d^+}} - \overline{\sqrt{P_d^-}}\right)^{-2} \quad \text{m}^2 \tag{32}$$

$$\text{low-SNR:} \quad \sigma_d^2 \geq \frac{c^2 T_s W N_0^2 B_L}{2\alpha(W)}\left(\overline{\sqrt{P_d^+}} - \overline{\sqrt{P_d^-}}\right)^{-4} \quad \text{m}^2. \tag{33}$$

Since the phase and delay measurements in the uplink and downlink parts of the link are independent, the variance of the two-way range error, σ_{ud}^2, can be expressed as the sum of the uplink and downlink range error variances: $\sigma_{ud}^2 = \sigma_u^2 + \sigma_d^2$; however, care must be taken to use the actual values of the signal powers and noise spectral densities in the uplink and downlink channels. The standard deviation of the two-way range error is shown in Figure 18, for the same set of parameters used in Figures 17 and 16, and further assuming that P_t/N_0 is the same in both the uplink and downlink channels. Note that the parameters selected for this example represent reasonable values for spacecraft and ground receivers, but do not correspond to bandwidth, modulation index, and chip durations used in the proof-of-concept experiments carried out in DTF-21, or deep-space PN ranging experiments carried out by New Horizons in 2012.

B. Comparison with DTF-21 Data

Four datasets recorded in September 2012 at DTF-21 were analyzed in detail, and the results presented in Section II-D. Here we compare the analysis results of the first

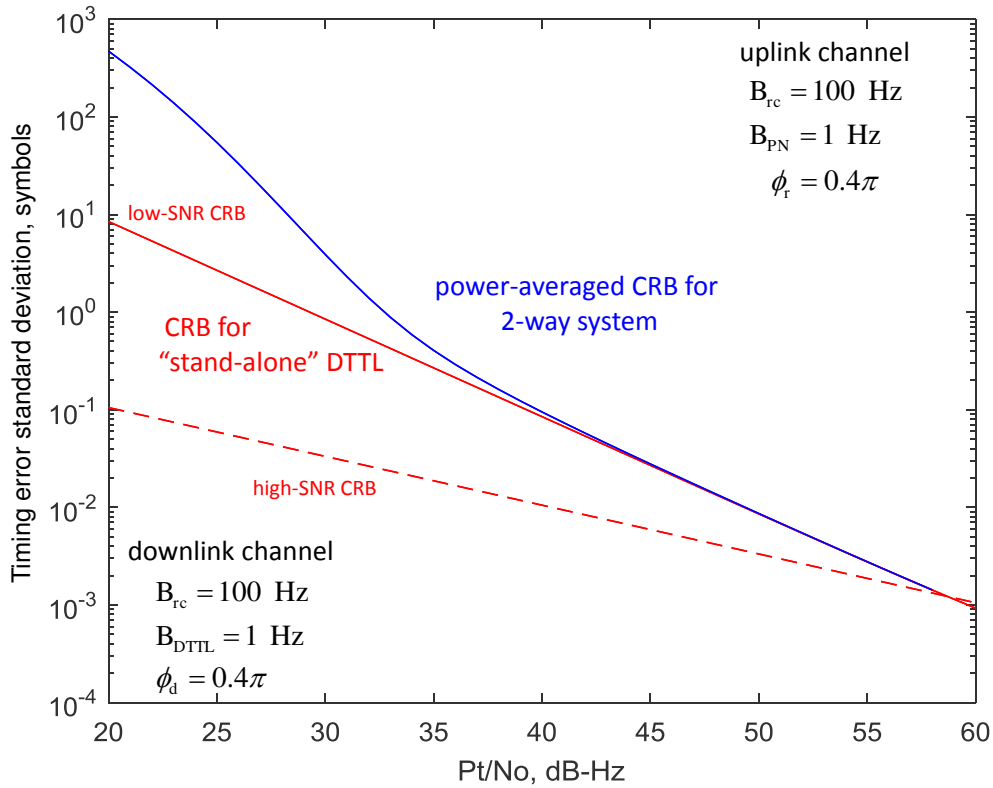

Figure 18. Performance of two-way ranging system, with independent uplink and downlink delay measurements, and $W = 1$.

dataset, designated as test run 262-0115 in Table 3 with theoretical predictions using the equations developed in this section.

The symbol rate for test run 262-0115 was 90.09014 ksym/s on the downlink channel, and the symbol SNR was $E_s/N_0 = 11.7$ dB, or $E_s/N_0 = 14.9$ natural units. The symbol duration corresponding to the symbol rate is $T_s = 1/(9.09014 \times 10^4) = 1.1001 \times 10^{-5}$ s, and the modulation index on the downlink was $\phi_d = 1.21$ radians, hence the relationship between total power and data power is $P_d = P_t \sin^2(\phi_d)$. The quantity of interest in tracking loop analysis is the ratio of data power to noise spectral density, which can be related to the symbol SNR as $P_d/N_0 = T_s^{-1} E_s/N_0$, yielding for this example $P_d/N_0 = (9.09014 \times 10^4) \times 14.9 = 1.35443 \times 10^6 = 61.317$ dB. In processing this data, a carrier loop bandwidth of 100 Hz was used, and the DTTL bandwidth was set at 10 Hz.

As can be seen in the red circle in Figure 19, the standard deviation of the DTTL delay estimates, in fractions of symbol duration, is 0.00192135 symbols at $P_d/N_0 = 61.317$ dB. Since one symbol duration is $T_s = 1.1001 \times 10^{-5}$ s, this rms error corresponds to 2.11368×10^{-8} s, or 21.1368 ns. This theoretical rms error is slightly lower than, but very close to the 22.8355 ns value reported in the data analysis subsection for the 262-0115 test run, which is shown as a black asterisk in Figure 19.

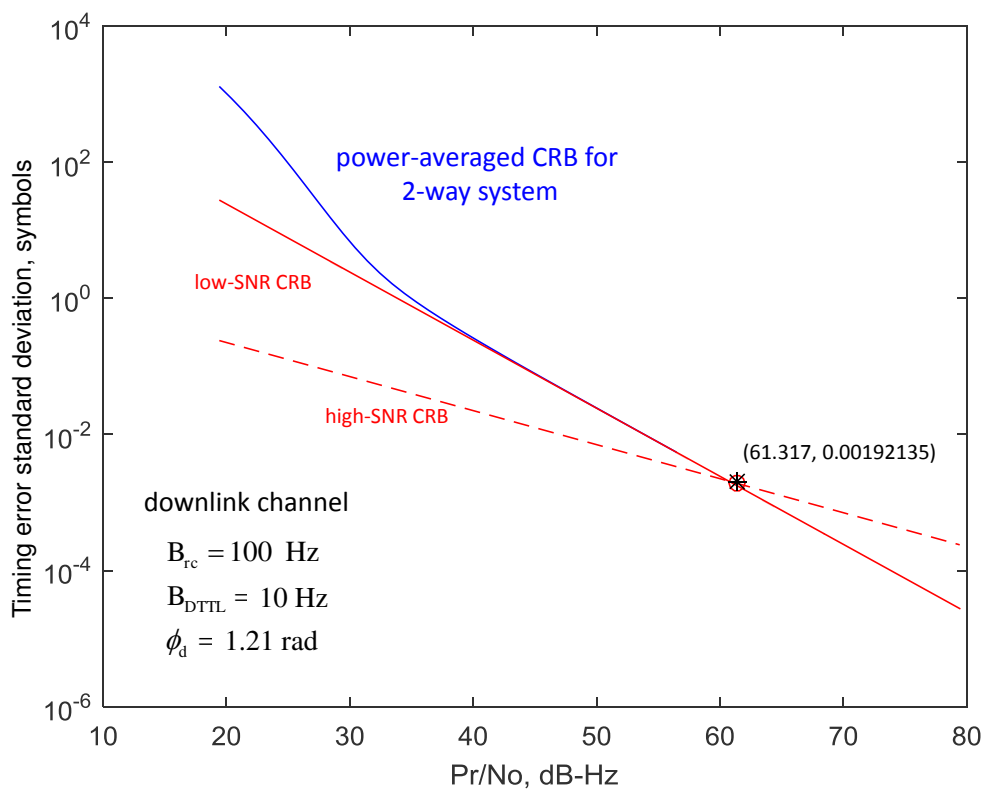

Figure 19. Fractional symbol error on the downlink channel as a function of P_d/N_0, corresponding to the analysis of DTF-21 data 262-0115.

As shown in Figure 5, an information block consisted of 1784 data-bits, which was randomized and encoded into a standard CCSDS rate 1/6 turbo code, hence the length of the encoded codeword is $(1784 + 4) \times 6 = 10728$ channel symbols. Each resulting codeword was of duration 0.119081 s, hence the codeword rate was 8.398 codewords per second. This implies that there are 255 complete codeword arrival times were reported in 30 s. The DTTL bandwidth was set to 10 Hz, hence independent samples are spaced $1/(2B_{\mathrm{DTTL}}) = 0.05$ s apart according to the Nyquist criterion. Since the coherence time of the DTTL output is 0.05 s but it is actually sampled once every 0.117688 s, or at time intervals that are 2.35 times greater than the coherence time, it is reasonable to assume that the codeword arrival-time samples are independent. Averaging 255 error samples reduces the standard deviation by $\sqrt{255} \approx 16$, hence the 30 s average of independent raw samples should theoretically yield $21.1368/16 = 1.32$ ns, which is somewhat lower than the measured value of 1.9415 ns. The reason for the discrepancy may be due to the bunching of the codeword arrival times around -2 ns and 3 ns evident in Figure 9, indicating the presence of systematic structure in the DTTL output that was not taken into account in this model, that tends to increase the standard deviation of the recorded data.

Additional averaging of the range estimates can be carried out during post-processing on the ground to further reduce the variance of the range error, depending on the accuracy of the range predicts. The results presented in this section refer to the fundamental range measurements carried out by the tracking loops on the spacecraft and on the ground, whose bandwidths (and hence effective averaging times) are often determined by external factors such as spacecraft hardware limitations or operational requirements on the ground.

The phase of the PN code transmitted on the uplink channel was recorded by sampling the NCO of the code-tracking loop in the Frontier Radio at the downlink codeword rate, and relayed to the ground on each subsequent codeword. These measurements are also subject to measurement error due to additive noise in the circuit, but as can be seen in Figure 7, there is a significant trend of unknown origin in the 30-s smoothed data that is clearly not due to additive noise. If this trend is removed by post-processing, the standard deviation of the residual measurement scatter in Figure 7 becomes approximately 0.005 chip of the PN code, where one PN code chip is 5×10^{-7} s for a 1-MHz range clock. The standard deviation of the residual scatter is approximately $0.005(5 \times 10^{-7}) \approx 2.5$ ns, which can be further reduced by a factor of 16 via 30-s averaging to 0.16 ns. When compared to the nearly 2 ns standard deviation of the codeword arrival times on the downlink channel, it is clear that the RSS of the uplink and downlink errors is dominated by the codeword arrival time errors, hence the contribution of the PN code phase measurement noise contributed by the Frontier Radio can be ignored in the DTF-21 tests.

C. Telemetry Ranging Performance as a Function of Bit-Rate

Telemetry ranging employs a PN code on the uplink, measures the PN code phase at the spacecraft, and reports this phase as part of downlink telemetry. We assume for this example that the uplink system is similar to the current architecture, which employs a PN code with a nominal 2-Mchip/s range clock component. However, the downlink telemetry is currently not limited to 2 Msps, and is expected to operate at much higher data rates in the future. The data link is designed to enable decoding at any rate. The downlink signal is taken to be residual carrier BPSK encoded with a rate-1/6 turbo code typically employed for deep space missions. The code requires the bit SNR to be 0 dB or greater, or $E_b/N_0 \geq 1$ in natural units, and hence the following equations establish the relationship between the required bit-rate for a rate-1/6 code: $1 = E_b/N_0 = 6E_s/N_0 = 6T_s(P_t/N_0) = (P_t/N_0)/R$, where E_s is the symbol energy, T_s is the symbol duration, and $R = 1/(6T_s)$ is the data rate in b/s. Note that while the uplink code chip rate is fixed via the 1-MHz range clock in this example, the downlink data rate increases linearly with P_t/N_0, since we imposed the constraint $E_s/N_0 = 1$ in order to close the link.

A plot of the two-way range error standard deviation as a function of data rate R is shown in Figure 20, with the assumptions that the modulation index is $\phi_r = \phi_d = 0.4\pi$ in both the uplink and the downlink. The bandwidths of the carrier tracking loop and PN code tracking loop on the spacecraft are 30 Hz and 0.25 Hz respectively. The downlink receiver on the ground uses a DPLL to track the carrier and a DTTL to track the data symbols, with respective bandwidths of 0.5 Hz and 0.05 Hz, as typical in DSN operations. It can be seen in Figure 20 that radio loss from the DPLL significantly degrades overall performance below 3 ksps, but has no impact on two-way ranging performance at data rates above 10-ksps. It can also be inferred that a data rate greater than about 2 kbps is sufficient to achieve 2 m rms two-way range error (or 1 m one-way range error) with the assumed link parameters. Even better performance is possible if the uplink parameters are optimized, and if suppressed carrier modulation is used on the downlink; however, a detailed study of these options is beyond the scope of this article.

IV. Conclusions

A set of tests of telemetry ranging were conducted at DTF-21, using the Frontier Radio. The Frontier Radio was able to successfully lock on the uplink range code, latch the range code phase at appropriate intervals, insert these values into downlink telemetry frames, and transmit turbo-encoded telemetry on the downlink. Open-loop recorders, in the form of an RSR, VSR, or PRSR, recorded the downconverted telemetry signals. Post-processing was able to receive, decode, and extract the spacecraft phase measurements. When the laboratory set-up was properly configured, post-processing of recorded data was able to identify time of arrival of the telemetry frames, to within 2.1 to 3.4 ns.

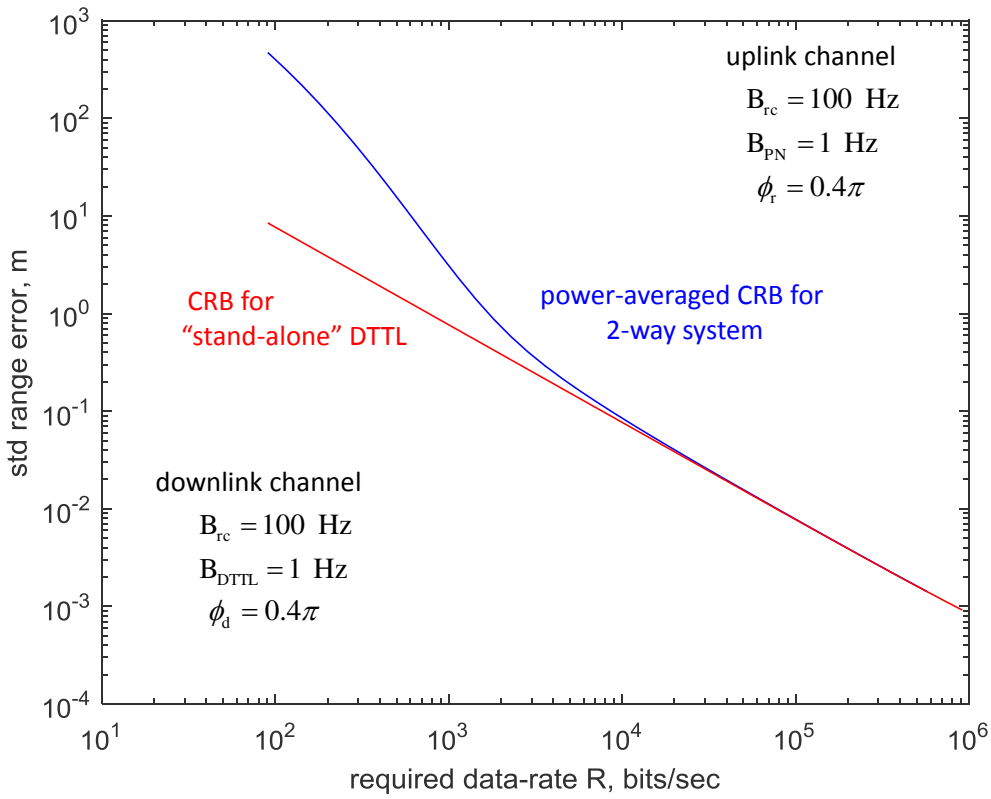

Figure 20. Two-way rms range error in meters, as a function of required data rate R in b/s.

These accomplishments validate the analytically derived performance of the uplink and downlink signal processing presented in [2]. End-to-end performance analysis is consistent with the observed variance of the end-to-end laboratory tests. For certain scenarios considered (rate-1/6 turbo code operating at threshold), the telemetry ranging approach is capable of resolving range to less than a meter when the data rate is more than 1 kbps. This suggests that telemetry ranging may be feasible and sufficiently accurate for typical deep space missions.

Acknowledgments

The authors are pleased to acknowledge Christopher Green, Mircea Metes, Mike Abbod, and Ronald Logan of Exelis, Inc., for help in planning and conducting the tests at DTF-21, Joseph Hennawy for coordinating the JHU/APL participation, and Sanjana Rajan for helping develop the software to post-process the test data.

References

[1] J. Hamkins, P. Kinman, H. Xie, V. Vilnrotter, and S. Dolinar, "Telemetry ranging: Concepts," *The Interplanetary Network Progress Report*, vol. 42-203, Jet Propulsion Laboratory, Pasadena, California, pp. 1–21, November 15, 2015.
http://ipnpr.jpl.nasa.gov/progress_report/42-203/203C.pdf

[2] J. Hamkins, P. Kinman, H. Xie, V. Vilnrotter, and S. Dolinar, "Telemetry ranging: Signal processing," *The Interplanetary Network Progress Report*, vol. 42-204, Jet Propulsion Laboratory, Pasadena, California, pp. 1–56, February 15, 2016.
http://ipnpr.jpl.nasa.gov/progress_report/42-204/204D.pdf

[3] J. Hennawy, N. Adams, E. Sanchez, D. Srinivasan, J. Hamkins, V. Vilnrotter, Hua Xie, and P. Kinman, "Telemetry ranging using software-defined radios," *Proceedings of the IEEE Aerospace Conference*, Big Sky, MT, pp. 1–14, March 2015.

[4] C.B. Haskins and W.P. Millard, "Multi-band software defined radio for spaceborne communications, navigation, radio science, and sensors," *Proceedings of the IEEE Aerospace Conference*, Big Sky, MT, pp. 1–9, March 2010.

[5] R.J. DeBolt, D.J. Duven, C.B. Haskins, C.C. DeBoy, T.W. LeFevere, "A regenerative pseudonoise range tracking system for the New Horizons spacecraft," *Proceedings of the 61st Annual Meeting of the Institute of Navigation*, Cambridge, MA, pp. 487–497, June 2005.

[6] P. Kinman, "Pseudo-Noise and Regenerative Ranging," *DSN Telecommunications Link Design Handbook*, DSN No. 810-005, module 214, Rev. A, Jet Propulsion Laboratory, Pasadena, California, October 28, 2015.
http://deepspace.jpl.nasa.gov/dsndocs/810-005/214/214A.pdf

[7] CCSDS 131.0-B-2, "TM synchronization and channel coding," Blue Book, Issue 2, Aug. 2011.
http://public.ccsds.org/publications/archive/131x0b2ec1.pdf

[8] W.C. Lindsey and M.K. Simon, *Telecommunication Systems Engineering*, Dover, Toronto, Ontario, 1973.

[9] J. Hamkins and M. Simon, *Autonomous Software-Defined Radio Receivers for Deep Space Applications*, Wiley-Interscience, Hoboken, N.J, 2006.

[10] J.R. Jensen, C.B. Haskins, and C.C. DeBoy, "Regenerative PN ranging experience with New Horizons during 2012," *Proceedings of the IEEE Aerospace Conference*, Big Sky, MT, pp. 1–7, March 2013.

[11] C.B. Haskins, "X-band digital receiver for the New Horizons spacecraft," *Proceedings of the IEEE Aerospace Conference*, Big Sky, MT, March 2004.